



A large conjugated rigid dimer acceptor enables 20.19% efficiency in organic solar cells†

Cite this: DOI: 10.1039/d5ee00878f

Wendi Shi,^{‡a} Qiansai Han,^{‡a} Wenkai Zhao,^b Ruohan Wang,^a Longyu Li,^a Guangkun Song,^a Xin Chen,^a Guankui Long,^{id b} Zhaoyang Yao,^{id a} Yan Lu,^{id c} Chenxi Li,^{*a} Xiangjian Wan,^{id *a} and Yongsheng Chen,^{id *a}

Non-fullerene acceptors with a large conjugated rigid skeleton are conducive to promoting low disorder and reducing non-radiative recombination loss (ΔE_{nr}), thereby improving open voltage (V_{oc}) in organic solar cells (OSCs). However, an unfavorable active layer morphology is often formed due to excessive aggregation of these acceptors, which leads to a low short-circuit current density (J_{sc}) and fill factor (FF), and significantly lower device efficiencies. In this study, we report a dimer acceptor, QD-1, featuring a large conjugated rigid skeleton that exhibits low energy disorder, small reorganization energy, and weakened electro-photon coupling. All of these factors contribute to a reduction in ΔE_{nr} and improved charge mobility. Benefiting from the above advantages as well as favorable fibrillar morphology, a binary OSC based on PM6:QD-1 showed high and balanced device parameters in V_{oc} , J_{sc} , and FF, resulting in a high power conversion efficiency (PCE) of 19.46%, which is the highest reported for binary OSCs utilizing dimer acceptors. Furthermore, by incorporating QD-1 into the PM6:BTP-eC9 system, a remarkable PCE of 20.19% was achieved, accompanied by an improvement in all three photovoltaic parameters, due to the optimized morphology of the active layer. Additionally, a module (13.5 cm²) based on the ternary system achieved a high PCE of 17.33%.

Received 14th February 2025,

Accepted 22nd April 2025

DOI: 10.1039/d5ee00878f

rsc.li/ees

Broader context

Non-fullerene acceptors with a large, rigid conjugated skeleton tend to exhibit low disorder, reduced non-radiative recombination loss (ΔE_{nr}), and improved open-circuit voltage (V_{oc}) in organic solar cells (OSCs). However, excessive aggregation of these acceptors can lead to an unfavorable active layer morphology, resulting in a lower short-circuit current density (J_{sc}), fill factor (FF), and significantly lower device efficiencies. Herein, we report a dimer acceptor, QD-1, featuring a large conjugated rigid skeleton. As expected, a reduced ΔE_{nr} and improved charge mobility were observed for QD-1. Additionally, the active layer exhibited a favorable fibrillar morphology. Due to these advantages, the binary OSC based on PM6:QD-1 achieved high and balanced device parameters for V_{oc} , J_{sc} , and FF, resulting in an outstanding power conversion efficiency (PCE) of 19.46%, which is the highest reported for binary OSCs using dimer acceptors. When QD-1 was incorporated into the PM6:BTP-eC9 blend, the PM6:BTP-eC9:QD-1 system achieved an impressive PCE of 20.19% due to the optimized morphology. The system also demonstrated enhanced thermal stability. Additionally, a module (13.5 cm²) based on the ternary system achieved a high PCE of 17.33%, which is at the leading level for large area modules. This study highlights the significant potential of large conjugated rigid dimer acceptors for achieving high-efficiency OSCs.

^a State Key Laboratory of Elemento-Organic Chemistry, Frontiers Science Center for New Organic Matter, Key Laboratory of Functional Polymer Materials, Institute of Polymer Chemistry, Tianjin Key Laboratory of Functional Polymer Materials, Nankai University, Tianjin 300071, China. E-mail: lichenxi@nankai.edu.cn, xjwan@nankai.edu.cn, yschen99@nankai.edu.cn

^b School of Materials Science and Engineering, National Institute for Advanced Materials, Nankai University, Tianjin 300350, China

^c School of Materials Science and Engineering, Tianjin Key Laboratory for Photoelectric Materials and Devices, Key Laboratory of Display Materials and Photoelectric Devices, Ministry of Education, Tianjin University of Technology, Tianjin 300384, China

† Electronic supplementary information (ESI) available. See DOI: <https://doi.org/10.1039/d5ee00878f>

‡ Wendi Shi and Qiansai Han contributed equally to this work.

Introduction

Organic solar cells (OSCs), which have emerged as a promising renewable energy technology, are known for their many merits, such as good solution processability, lightweight, flexibility, and semi-transparency.^{1–4} In recent years, there has been rapid development of OSCs, and the power conversion efficiencies (PCEs) of single-junction devices have currently exceeded 20% due to innovations in molecular structure and progress in device engineering.^{5–14} However, compared to Si-based and perovskite-based solar cells, the PCEs of OSCs continue to lag behind.

This is caused by many factors, particularly the flexible molecular skeleton of organic materials, which leads to strong electron-phonon coupling. This causes increased non-radiative recombination and decreased OSC device open voltage (V_{oc}).^{15,16} Additionally, loose intermolecular aggregation generally results in large structural defects and amorphous phases. These defects and disorders can serve as recombination centers for excitons and charge carriers, leading to large trap state densities, low carrier mobilities, and decreased J_{sc} and fill factor (FF) in OSC devices.^{17–19}

At the single-molecule level, enhancing molecular rigidity through rational molecular design is an efficient strategy to address the above issues.^{20–24} A common strategy for designing organic semiconductor materials involves synthesizing large conjugated molecules by inserting two-dimensional (2D) conjugated aromatic rings into the molecular backbone. This approach is based on the fact that extending conjugation can enhance the molecular rigidity, thereby reducing the Urbach energy (E_u) and reorganization energy, weakening the electron-phonon coupling, and thus decreasing ΔE_{nr} and increasing charge mobility. In addition, compared to one-dimensional (1D) conjugation, 2D conjugation can strengthen the intermolecular interaction and improve the electronic coupling and charge transfer capabilities, which assists in reducing disorder and trap densities.^{25–28}

In recent years, dimers based on the Y6 skeleton have been widely studied and show promising photovoltaic performance and excellent stability. Various connection modes for synthesizing

these dimers have been reported in the literature, such as ‘end–end’ type,^{29–31} ‘center–center’ type,^{32,33} ‘shoulder–shoulder’ type,³⁴ and ‘alkyl–alkyl’ type.³⁵ However, most of these dimers are connected by small aryl or alkyl chains, which fail to form planar or rigid conjugates. While several research groups have synthesized dimers through rigid conjugate extension, the photovoltaic performance of these dimer-based binary devices falls behind that of other types of dimers due to poor J_{sc} and FF.^{21,36–38}

Recently, our group synthesized a series of acceptor molecules (CH-series) by central core conjugate extension.³⁹ These acceptors exhibit excellent properties, such as small values of E_u and low reorganization energy, which were attributed to 2D conjugation-extended backbones that enhance molecular rigidity and intermolecular π – π packing. In this study, based on the CH-series molecular design concept, we further extended molecular conjugations to synthesize a dimer acceptor, named QD-1 (Fig. 1a). Due to its large conjugated rigid molecular backbone, QD-1 exhibits a small reorganization energy, weak electron–photon coupling with a low Huang–Rhys parameter (S), and reduced energy disorder. Additionally, when PM6 was used as the donor, the active layer of the PM6:QD-1 blend displayed a smooth film surface and a distinct fibrillar morphology.

Benefiting from these advantages, the binary OSC based on PM6:QD-1 achieved a power conversion efficiency (PCE) of 19.46%, with a high V_{oc} of 0.895 V, J_{sc} of 27.52 mA cm^{–2}, and FF of 79.01%, which is the highest efficiency reported thus far for binary cells based on dimer acceptors. Furthermore, the ternary device based on the PM6:BTP-eC9:QD-1 system

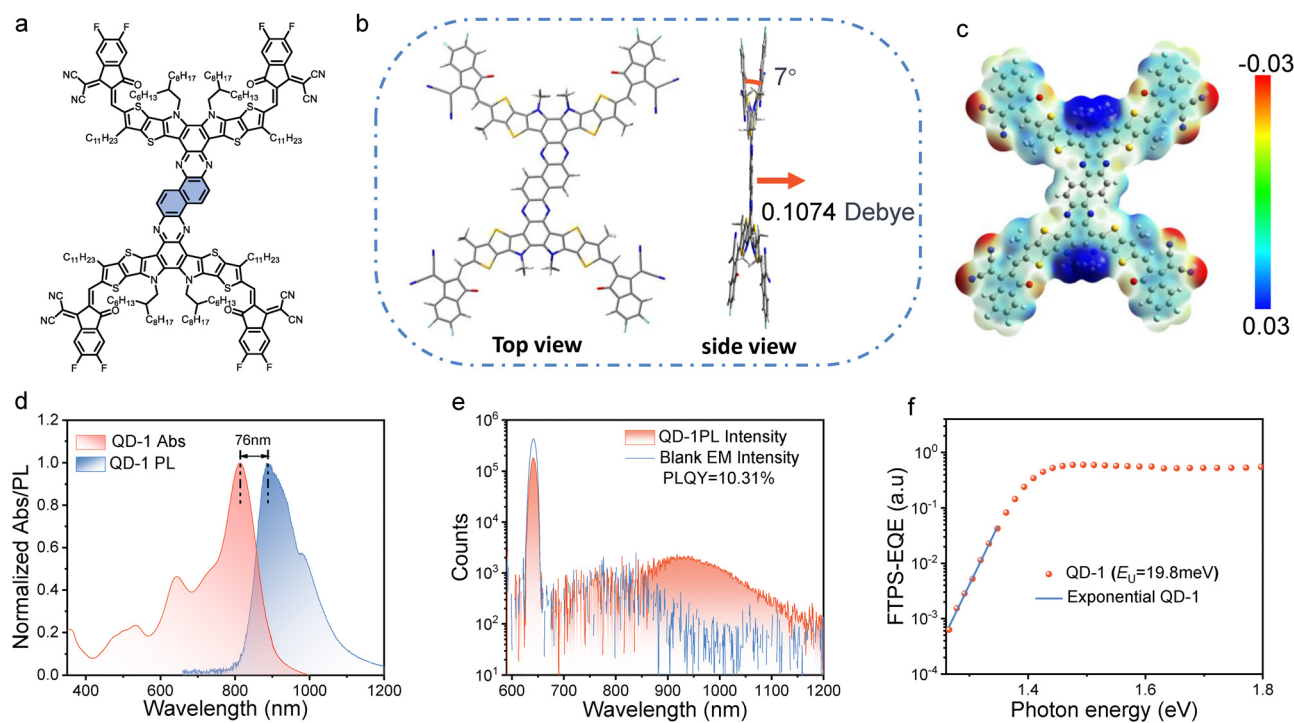


Fig. 1 (a) Chemical structures of QD-1. (b) Optimized molecular configuration of QD-1 through DFT calculation (B3LYP/6-31G level). (c) The electrostatic surface potential contour of QD-1. (d) UV-vis absorption (abs.) spectra of QD-1 in the film and photoluminescence (PL) spectra under 640 nm excitation. (e) Photoluminescence quantum yield of QD-1 film. (f) FTSP-EQE of the QD-1-based devices at the absorption onset.

achieved a remarkable PCE of 20.19% that was attributed to the optimized morphology with enhanced exciton dissociation, improved charge transport, and suppressed charge recombination following the incorporation of QD-1. Additionally, using the ternary system, a module with an effective area of 13.5 cm² was fabricated and exhibited an outstanding PCE of 17.33%.

Results and discussion

The synthetic route for QD-1 is outlined in Schemes S1–S3 (ESI[†]), with detailed synthesis procedures and characterization data provided in the ESI[†]. Due to the large rigid conjugated skeleton of QD-1, it demonstrates high thermal stability, with a decomposition temperature (T_d) of 354 °C, as determined by thermal gravimetric analysis (TGA) (Fig. S1, ESI[†]). The result of differential scanning calorimetry (DSC) is shown in Fig. S2 (ESI[†]). Density functional theory (DFT) calculations reveal a highly planar skeletal structure for QD-1 (Fig. 1b). As shown in the side view, the torsion angle for QD-1 is only 7°, indicating its near-planar geometry. The planar structure is beneficial for the formation of efficient intermolecular packings. The ground-state dipole moment (μ_g) of the model molecules was also analysed. The QD-1 shows a small μ_g of 0.1074 Debye that was due to its high molecular centrosymmetric structure.⁴⁰ Notably, the dipole moment for QD-1 is oriented perpendicular to the molecular backbone.

These properties are beneficial for enhancing intermolecular interactions while preventing excessive molecular aggregations, and also facilitating charge transport, thereby improving photovoltaic performance. The theoretical highest occupied molecular orbital (HOMO) and lowest unoccupied molecular orbital (LUMO) are primarily located on the electron-enriched central unit and electron-deficient terminals, respectively. The HOMO and LUMO for QD-1 are –5.58 eV and –3.58 eV, respectively (Fig. S3, ESI[†]). The surface electrostatic potential (ESP) was simulated, as displayed in Fig. 1c, and the majority of QD-1's surface exhibits positive ESP, indicating its electron affinity characteristics.

As shown in Fig. S4 (ESI[†]), QD-1 neat film exhibits a maximum absorption peak at 813 nm, which shows a redshift of 68 nm compared to its absorption in chloroform solution, indicating strong intermolecular π – π interactions. Moreover, as evidenced in Fig. S5 (ESI[†]), QD-1 shows low reorganization energies for holes (89.94 meV) and electrons (81.75 meV). A small reorganization energy is beneficial for reducing the driving force of exciton dissociation and improving charge mobility according to Marcus charge-transfer theory.⁴¹ The small reorganization energy of QD-1 was also confirmed by the narrow Stokes shift. As shown in Fig. 1d and Fig. S6 (ESI[†]), the Stokes shift value of QD-1 neat film is only 76 nm, which is smaller than that of most Y6 derivative acceptors.^{42,43} We also estimated the S value, a parameter of indication for electron–phonon coupling, using the equation $\Delta E_{\text{Stokes}} = 2S\hbar\omega$.^{44–46} As shown in Table S1 (ESI[†]), the S value of the QD-1 film is 0.433, which is much lower than that of Y6 (0.646) and BTP-eC9

(0.530), suggesting weakening electron–phonon coupling for QD-1.^{47,48} Therefore, the QD-1 neat film showed a high photoluminescence quantum yield (PLQY) of 10.31% (Fig. 1e). These results are conducive to decreasing the ΔE_{nr} in an OSC device.

Notably, the low energy disorder of materials can also decrease the ΔE_{nr} in OSCs under light and facilitate charge extraction and transport.^{20,49} Therefore, we measured E_u by Fourier transform photocurrent spectroscopy-external quantum efficiency (FTPS-EQE) to quantify the energy disorder. As shown in Fig. 1f, QD-1 exhibits a low E_u of 19.8 meV, which indicates low energy disorder and trap density in the film. This favours suppressing charge recombination and improving carrier mobilities.

Grazing incidence wide-angle X-ray scattering (GIWAXS) was used to study the intermolecular packing morphology of QD-1 neat film. As shown in Fig. S7 (ESI[†]) and summarized in Table S2 (ESI[†]), the QD-1 neat film exhibits a strong π – π stacking (010) diffraction peak in the out-of-plane (OOP) direction at 1.64 Å^{–1} ($d = 3.83$ Å) and a strong lamellar peak (100) in the in-plane (IP) direction at 0.348 Å^{–1} ($d = 18.06$ Å), indicating a predominance of face-on orientation. These results suggest that ordered intermolecular packing is a characteristic of QD-1, and it contributes to its high electron mobility, with an average value of 5.89×10^{-4} cm² V^{–1} s^{–1} (Fig. S8, ESI[†]).

The UV-vis absorption spectra demonstrate that the absorption characteristics of QD-1 are complementary with those of PM6 (Fig. S9a, ESI[†]), while BTP-eC9 (Fig. S9b, ESI[†]) exhibits an absorption range broader than that of QD-1, as illustrated in Fig. 2a. Cyclic voltammetry (CV) was conducted to estimate the energy levels of QD-1. The CV curves were used to determine the HOMO and LUMO energy levels of QD-1, which were –5.73 and –3.80 eV, respectively (Fig. 2b and Fig. S10, ESI[†]). Compared to those of BTP-eC9,⁵⁰ the HOMO energy level of QD-1 is lower and the LUMO energy level is higher, with a larger bandgap of 1.93 eV.

Then, PM6 was selected as a polymer donor to investigate the photovoltaic performance of QD-1 as a host acceptor and guest acceptor. The device structure of the solar cell is ITO/2PACz/Active layer/PNDIT-F3N/Ag. After device optimization, the PM6:QD-1-based device achieved an impressive PCE of 19.46%, with a V_{oc} of 0.895 V, a J_{sc} of 27.52 mA cm^{–2}, and an FF of 79.01% (Table 1 and Fig. 2c). To the best of our knowledge, this is the highest PCE achieved for binary devices based on dimer acceptors (Fig. 2f and Table S3, ESI[†]).

To further improve the efficiency, we fabricated a ternary device using a more redshifted acceptor, BTP-eC9. Moreover, when 20% QD-1 was incorporated as the guest acceptor, the ternary device achieved a substantially higher PCE of 20.19%, accompanied by an improved V_{oc} of 0.873 V, J_{sc} of 28.98 mA cm^{–2}, and FF of 79.82%, which surpassed the PCE of PM6:BTP-eC9 (19.53%). Fig. 2d shows the external quantum efficiency (EQE) curves of the binary and ternary devices. The integrated current densities of PM6:QD-1, PM6:BTP-eC9, and PM6:BTP-eC9:QD-1 were calculated as 26.52, 27.31, and 27.96 mA cm^{–2}, respectively, matching well with that measured from the current density–voltage (J – V) test. Furthermore, these

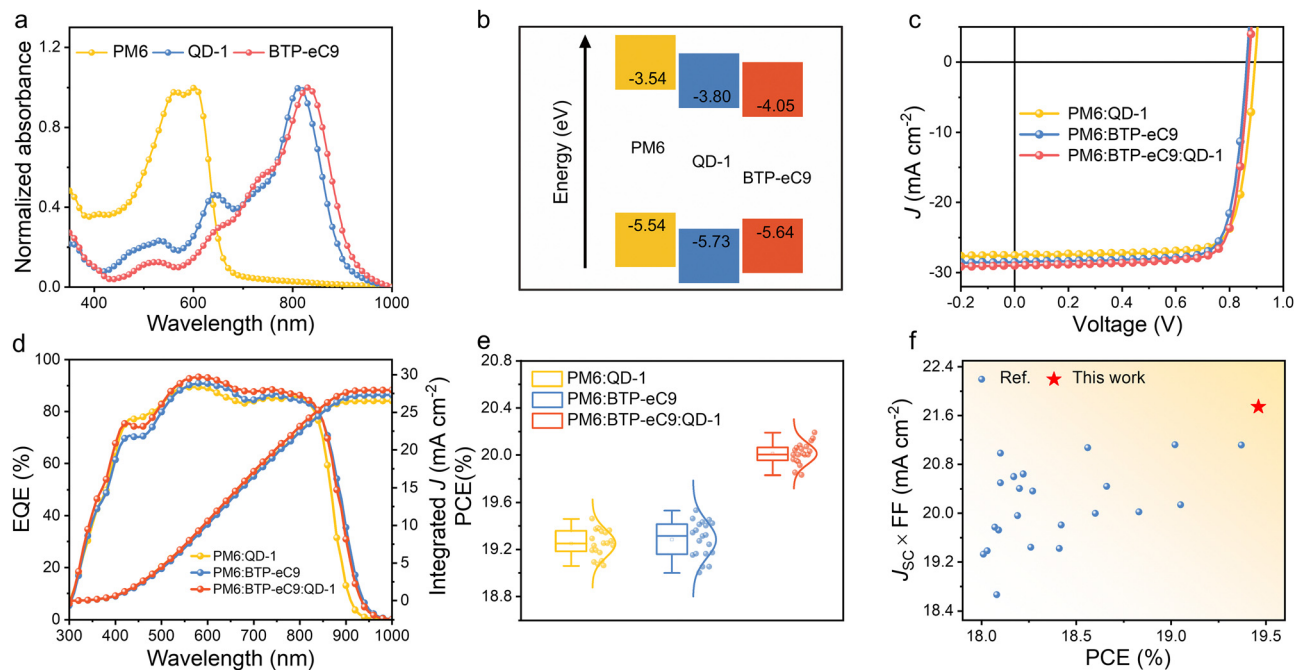


Fig. 2 (a) Normalized absorption spectra of PM6, BTP-eC9, and QD-1 in solid films. (b) The alignment of energy levels. (c) J - V curves for OSCs. (d) EQE plots and integrated J_{sc} curves. (e) Statistical histograms of PCEs of OSCs based on PM6:QD-1, PM6:BTP-eC9, and PM6:BTP-eC9:QD-1. (f) $J_{sc} \times FF$ as a function of PCE of the binary OSCs based on QD-1 and the OSCs with a PCE > 18% in the literature. Source references for the data points are provided in Table S3 (ESI[†]).

Table 1 Summary of photovoltaic parameters for OSCs

Active layers	V_{oc} (V)	J_{sc} (mA cm^{-2})	J_{sc}^{EQE}	FF	PCE ^a (%)
PM6:QD-1	0.895 (0.890 \pm 0.003)	27.52 (27.54 \pm 0.17)	26.52	79.01 (78.53 \pm 0.43)	19.46 (19.25 \pm 0.11)
PM6:BTP-eC9	0.864 (0.858 \pm 0.006)	28.51 (28.31 \pm 0.25)	27.31	79.30 (79.42 \pm 0.28)	19.53 (19.28 \pm 0.15)
PM6:BTP-eC9:QD-1	0.873 (0.868 \pm 0.004)	28.98 (28.89 \pm 0.25)	27.96	79.82 (79.83 \pm 0.66)	20.19 (20.01 \pm 0.09)

^a The average values in parentheses were obtained from 20 independent devices.

devices exhibited excellent reliability, as evidenced by testing 20 independent devices, with the statistical representation depicted in Fig. 2e.

To determine why the PCEs for QD-1-based OSCs were high, a comprehensive study of excitons along with charge dynamic analysis was conducted. First, we studied the charge generation and dissociation process by exploring the photocurrent density (J_{ph}) versus effective voltage (V_{eff}).⁵¹ As depicted in Fig. 3a, under the short-circuit condition and maximum power output conditions, the exciton dissociation efficiency (P_{diss}) and charge extraction efficiency (P_{coll}) of the PM6:QD-1-, PM6:BTP-eC9-, and PM6:BTP-eC9:QD-1-based OSCs are 98.44%/89.15%, 97.41%/90.48%, and 98.30%/92.17%, respectively. The higher P_{diss} and P_{coll} suggest that the ternary device possesses exciton dissociation and charge collection properties with greater efficiency compared with the PM6:BTP-eC9-based binary device, which contributed to the higher J_{sc} and FF of the QD-1-based ternary device.

Next, we measured the light intensity (P_{light})-dependent J_{sc} to investigate the charge recombination under the short-circuit condition.⁵² As shown in Fig. 3b, the slopes of the J_{sc} versus

light intensity curve (α) for the PM6:QD-1 and PM6:BTP-eC9:QD-1 devices were 0.991 and 0.993, respectively, which are higher than that of PM6:BTP-eC9 (0.990). According to the power-law equation $J_{sc} \propto P_{light}^\alpha$, as α becomes closer to 1, the bimolecular recombination becomes smaller. Thus, the results suggest that the introduction of QD-1 contributed to the inhibition of bimolecular recombination.

The transient photocurrent (TPC) and transient photovoltage (TPV) tests (Fig. 3c and Fig. S11, ESI[†]) revealed that the charge extraction time decreased in the order of PM6:QD-1 (0.40 μs), PM6:BTP-eC9 (0.35 μs), and PM6:BTP-eC9:QD-1 (0.26 μs), while the photogenerated carrier lifetime increased from 69 μs to 100 μs and then to 115 μs . The shorter charge extraction time and longer carrier lifetime in the ternary device contributed to higher carrier mobility and less charge carrier recombination.

Carrier mobility was further investigated using the space charge limited current (SCLC) method (Fig. 3d and Fig. S12, ESI[†]). The electron (μ_e) and hole mobilities (μ_h) of the PM6:QD-1, PM6:BTP-eC9, and PM6:BTP-eC9:QD-1 blends were estimated to be $7.33 \times 10^{-4}/6.27 \times 10^{-4} \text{ cm}^2 \text{ V}^{-1} \text{ s}^{-1}$, $7.54 \times 10^{-4}/6.54 \times 10^{-4} \text{ cm}^2 \text{ V}^{-1} \text{ s}^{-1}$, and $8.65 \times 10^{-4}/7.56 \times 10^{-4} \text{ cm}^2 \text{ V}^{-1} \text{ s}^{-1}$,

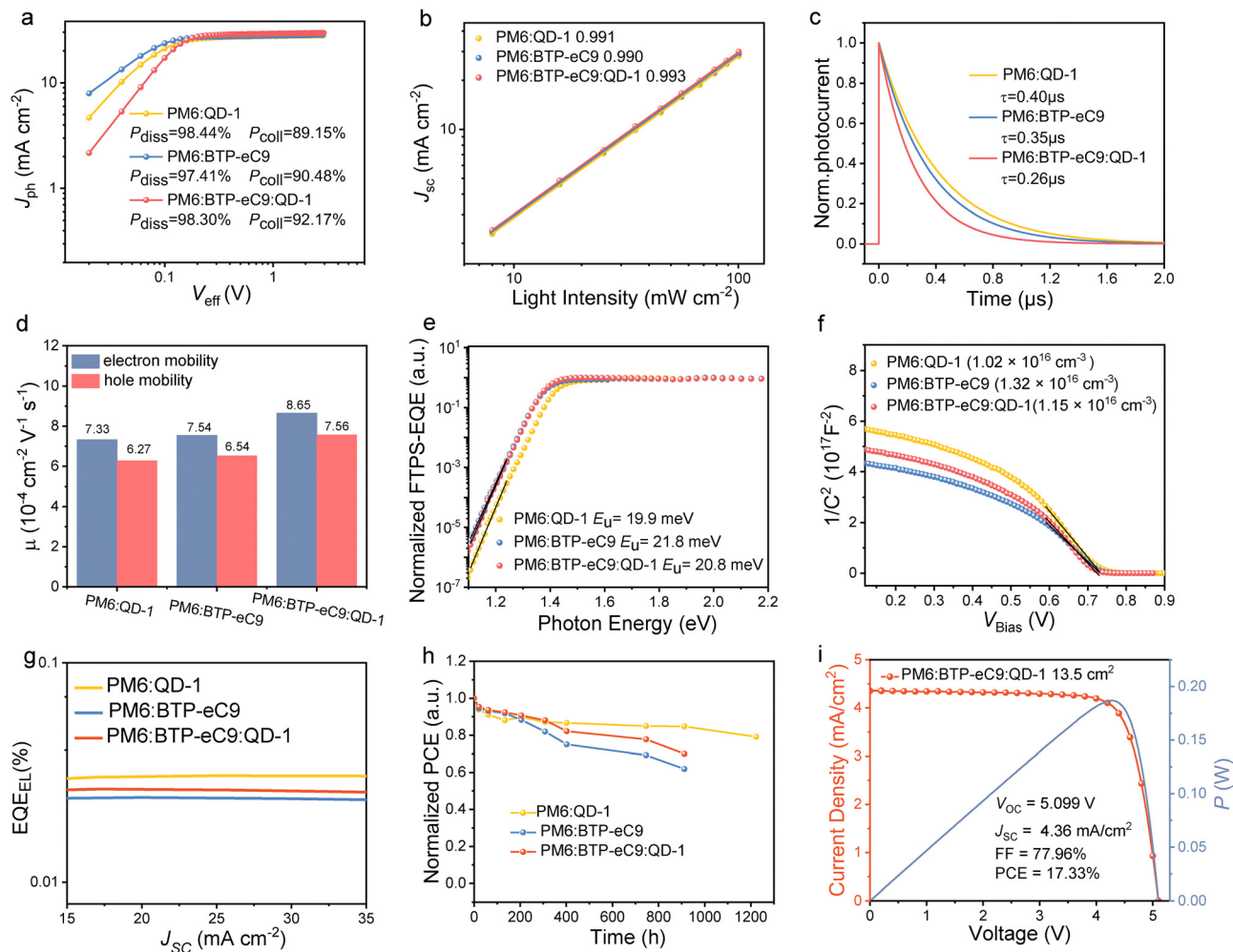


Fig. 3 (a) J_{ph} versus V_{eff} curves indicating P_{diss} and P_{coll} . (b) Light intensity (P_{light}) dependence of J_{sc} . (c) Transient photocurrent measurement of binary and ternary devices. (d) The electron and hole mobilities of the PM6:QD-1, PM6:BTP-eC9, and PM6:BTP-eC9:QD-1 blends acquired from single-carrier devices. (e) FTPS-EQE of the PM6:QD-1, PM6:BTP-eC9, and PM6:BTP-eC9:QD-1 devices at the absorption onset. (f) Mott-Schottky plots (dashed lines represent the linear fitting). (g) The corresponding EQE_{EL} spectra for the optimized OSCs. (h) Thermal stability of the PM6:QD-1-, PM6:BTP-eC9-, and PM6:BTP-eC9:QD-1-based OSCs without encapsulation in a nitrogen-filled glove box at 65 °C. (i) $J-V$ and $P-V$ curves of the PM6:BTP-eC9:QD-1 module.

with μ_e/μ_h of 1.17, 1.15, and 1.14, respectively. The higher and more balanced charge transport values contributed to the higher FF and J_{sc} of ternary OSC compared with the binary OSCs.

The E_u of blend films was also measured by fitting the low photon energy region from the FTPS-EQE spectrum. The E_u values for PM6:QD-1, PM6:BTP-eC9, and PM6:BTP-eC9:QD-1 are 19.9, 21.8, and 20.8 meV, respectively (Fig. 3e). The small E_u values suggest that the energetic disorder for the PM6:QD-1-based device is low, and the addition of QD-1 can effectively decrease the energetic disorder in the ternary device. We characterized trap density using capacitance measurements at various bias voltages. From the Mott-Schottky plot (Fig. 3f), the trap densities of PM6:QD-1, PM6:BTP-eC9, and PM6:BTP-eC9:QD-1 are $1.02 \times 10^{16} \text{ cm}^{-3}$, $1.32 \times 10^{16} \text{ cm}^{-3}$, and $1.15 \times 10^{16} \text{ cm}^{-3}$, respectively, suggesting that the introduction of QD-1 can effectively reduce the defect state of the film and

inhibit molecular disorder. The detailed energy loss (E_{loss}) analysis results are presented in Table S4 (ESI[†]).

The optical bandgap (E_g) and EQEs of electroluminescence (EQE_{EL}) for the PM6:QD-1-, PM6:BTP-eC9- and PM6:BTP-eC9:QD-1-based OSCs are displayed in Fig. S13 (ESI[†]) and Fig. 3g. The ΔE_{nr} of OSCs were calculated to be 0.209, 0.215, and 0.213 eV, respectively. The reduced ΔE_{nr} observed in QD-1-based OSCs can be attributed to its weak electron-phonon coupling, small reorganization energy, low energy disorder, and trap density.

To explore the stability of QD-1-based devices, we measured their thermal stability and photo-stability. As shown in Fig. 3h, the PM6:QD-1 device exhibited a T80 lifetime of approximately 1200 h after annealing at 65 °C in a nitrogen atmosphere. The T80 lifetimes of the PM6:BTP-eC9:QD-1 device and PM6:BTP-eC9 device are 570 h and 330 h, respectively. The results show that incorporating QD-1 into the PM6:BTP-eC9 active layer can

improve the thermal stability. The photo-stability of the unpackaged devices was measured at the maximum power point (MPP) under continuous 100 mW cm^{-2} light illumination. As shown in Fig. S14 (ESI[†]), the PCE of the PM6:QD-1 device decreased to 60% of its initial value after 400 h. The stability improvement may be attributed to the large conjugated structure of QD-1, which assists in maintaining the morphology of the active layer by suppressing the diffusion of acceptor molecules.

Based on the PM6:BTP-eC9:QD-1 ternary blend, a module comprising six sub-cells connected in series, with an effective area of 13.5 cm^2 , was successfully fabricated. The module's structure is glass/ITO/PEDOT:PSS/PM6:BTP-eC9:QD-1/PNDIT-F3N/Ag (Fig. S15, ESI[†]). A photograph of the module is shown in Fig. S16 (ESI[†]). The J - V curve is presented in Fig. 3i. The optimal module exhibited an impressive PCE of 17.33%, with a V_{oc} of 5.099 V, a J_{sc} of 4.36 mA cm^{-2} , and an FF of 77.96%. To the best of our knowledge, this PCE value is one of the highest ever reported for an organic solar module. This result underscores the significant potential of large conjugated rigid dimer acceptors in practical applications.

To explore the relationship between the morphology of the active layer and device performance of OSCs, we first employed atomic force microscopy-based infrared (AFM-IR) spectroscopy to investigate the surface morphology differences among the three systems. As depicted in Fig. S17 and S18 (ESI[†]),

the root-mean-square (RMS) roughness of the three blend films is approximately 0.7 nm, indicating uniform and smooth film surfaces. In addition, all three blend films showed distinct fiber-like network structures, which facilitate charge recombination reduction and enhance carrier transport.

Next, we detected the characteristic absorption peak (2216 cm^{-1}) of the $\text{C}\equiv\text{N}$ bond in acceptors to record AFM-IR signals from the blend films. As shown in Fig. 4a, a clear fibrillar network morphology of the donor and acceptor interpenetrating structure appears at the nanoscale level in all three systems. Notably, PM6:QD-1 showed relatively larger phase separation, while PM6:BTP-eC9 exhibited smaller phase separation, and PM6:BTP-eC9:QD-1 showed moderate phase separation. More favorable phase separation in the ternary OSC contributed to higher J_{sc} and FF. The statistical analysis of nanofiber sizes is presented in Fig. S19 (ESI[†]) and Fig. 4b. The fiber sizes of PM6:QD-1, PM6:BTP-eC9:QD-1, and PM6:BTP-eC9 gradually increased from 8.51 nm, 11.85 nm, to 13.87 nm respectively, indicating moderate molecular crystallinity for PM6:BTP-eC9:QD-1. The more favorable crystallinity of the ternary film promoted carrier transport and reduced the charge recombination.

The average ESP value further supports the above results. As shown in Figs S20 to S22 (ESI[†]), QD-1 exhibited a reduced average ESP value of $5.397 \text{ kcal mol}^{-1}$ as compared to that of BTP-eC9 ($5.414 \text{ kcal mol}^{-1}$), leading to weakened interaction

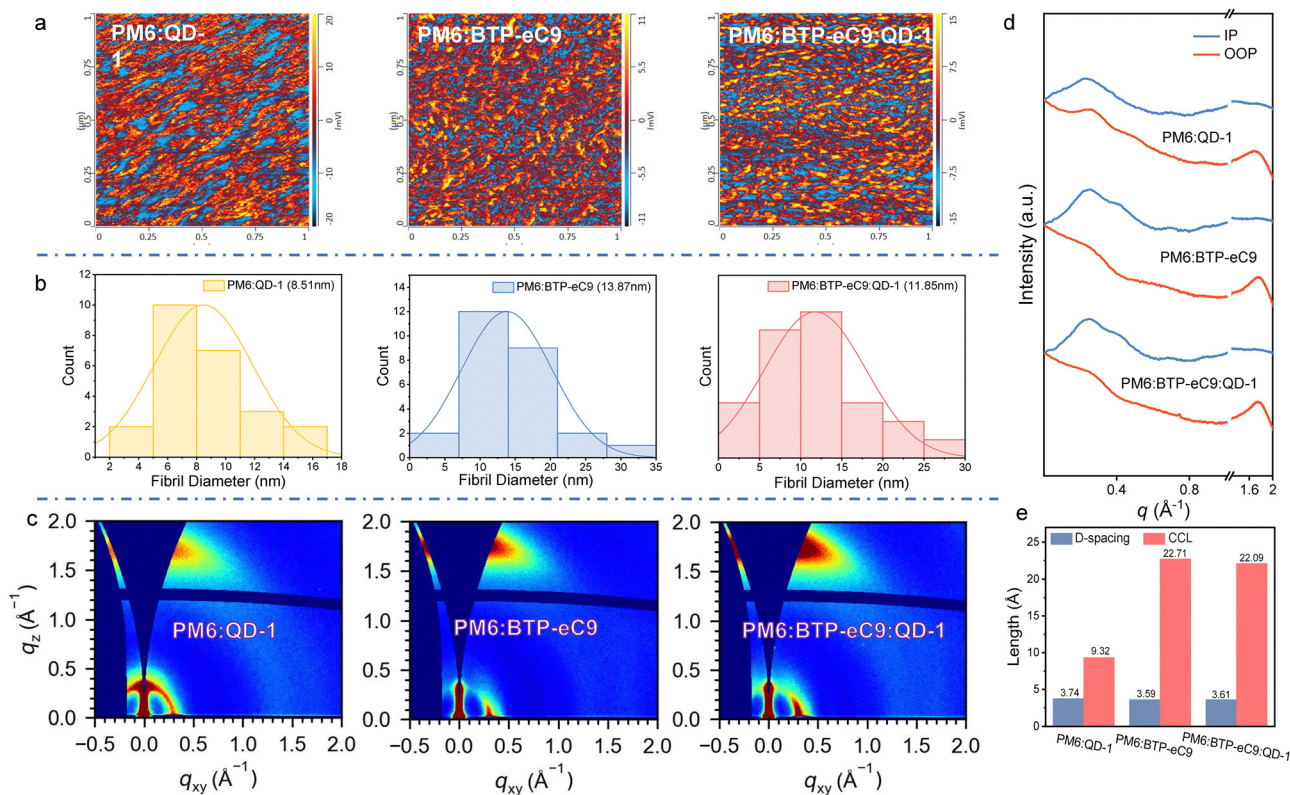


Fig. 4 (a) AFM-IR phase images of the three blended films by measuring the 2216 cm^{-1} signal of acceptors, in which donor and acceptor domains were marked with blue and red colors, respectively. (b) Statistical distribution of fibril diameters. (c) 2D GIWAXS patterns of blended films. (d) Extracted line-cut profiles from 2D GIWAXS patterns of blended films. (e) D-spacing and crystal coherence length (CCL) in the π - π stacking direction (010) in blended films from GIWAXS tests.

between donor PM6 and QD-1. The donor/acceptor (D/A) phase separation size is usually closely related to the miscibility between donor and acceptor, and therefore, we derived the corresponding Flory–Huggins interaction parameters (χ) from the results of the contact angle measurements. The smaller the χ value, the better the miscibility.

As displayed in Fig. S23 and Table S5 (ESI[†]), PM6:QD-1 possesses a relatively larger $\chi_{\text{PM6:QD-1}}$ of 0.033, indicating weaker D/A miscibility and larger phase-separated morphology. In contrast, $\chi_{\text{PM6:BTP-eC9}}$ exhibited a smaller value of 0.026, suggesting better miscibility, which is also consistent with its smaller phase separation. The $\chi_{\text{PM6:BTP-eC9:QD-1}}$ (0.031) lies between these values, indicating that the introduction of QD-1 reduced the miscibility of PM6 and BTP-eC9, which is one of the reasons for the moderate phase separation observed in the ternary system.

The molecular packing and crystallinity in the three blended films were further investigated using GIWAXS (Fig. 4c, d, and Table S6, ESI[†]). All the blended films exhibited strong (010) diffraction peaks, at 1.68 \AA^{-1} for PM6:QD-1, 1.75 \AA^{-1} for PM6:BTP-eC9, and 1.74 \AA^{-1} for PM6:BTP-eC9:QD-1 in OOP directions, and sharp (100) diffraction peaks at 0.298 \AA^{-1} for PM6:QD-1, 0.308 \AA^{-1} for PM6:BTP-eC9, and 0.306 \AA^{-1} for PM6:BTP-eC9:QD-1 in IP directions, demonstrating the preferential face-on orientation.

Furthermore, in the OOP direction (Fig. 4e), PM6:BTP-eC9 exhibited more compact stacking distances of 3.59 \AA and stronger film crystallization (higher CCL of 22.71 \AA) compared with PM6:BTP-eC9:QD-1 (stacking distances of 3.61 \AA and CCL of 22.09 \AA). This indicates that the addition of QD-1 suppresses

excessive stacking and decreases crystallinity, thereby assisting in the formation of a more ideal morphology for the ternary blend film. Conversely, PM6:QD-1 exhibited the weakest crystallinity, which was evidenced by the smallest CCL of 9.32 \AA . Moreover, the stacking distance of PM6:QD-1 exhibited a relatively high value of 3.74 \AA . It is not conducive to charge transport, and may be one of the reasons for the relatively lower FF compared with that of the ternary device.

Femtosecond transient absorption (TA) spectroscopy was employed to understand exciton kinetics in the blend films. The acceptor molecules were selectively excited by a pump pulse wavelength of 800 nm for the PM6:QD-1, PM6:BTP-eC9, and PM6:BTP-eC9:QD-1 blends. The time-resolved 2D color TA spectra of the PM6:QD-1, PM6:BTP-eC9, and PM6:BTP-eC9:QD-1 films are shown in Fig. 5a and Fig. S24 (ESI[†]). After excitation, the PM6:QD-1 blend exhibited ground state bleaching (GSB) of QD-1 at 820 nm , and excited-state absorption (ESA) at 910 nm . Similarly, the PM6:BTP-eC9 and PM6:BTP-eC9:QD-1 blends exhibited GSB and ESA of BTP-eC9 at approximately 830 and 920 nm , respectively. All blends showed a GSB of PM6 in the range between 580 and 630 nm , and an ESA at 1550 nm . The ESA at 1550 nm exhibited the characteristic feature of the intramoiety excimer (i - EX) state of Y-series acceptors, which is derived from the primary local excitation (LE) state.⁵³

From the plot of the TA profiles at various delay times (Fig. 5b and Fig. S25, ESI[†]), it is evident that the bleaching peak ($820 \text{ nm}/830 \text{ nm}$) of the acceptor (QD-1/BTP-eC9) decreases with the extension of time, while the GSB peak ($580\text{--}630 \text{ nm}$) of PM6 increases, indicating an effective hole-transfer process from the acceptor to PM6. To evaluate the hole transfer processes in

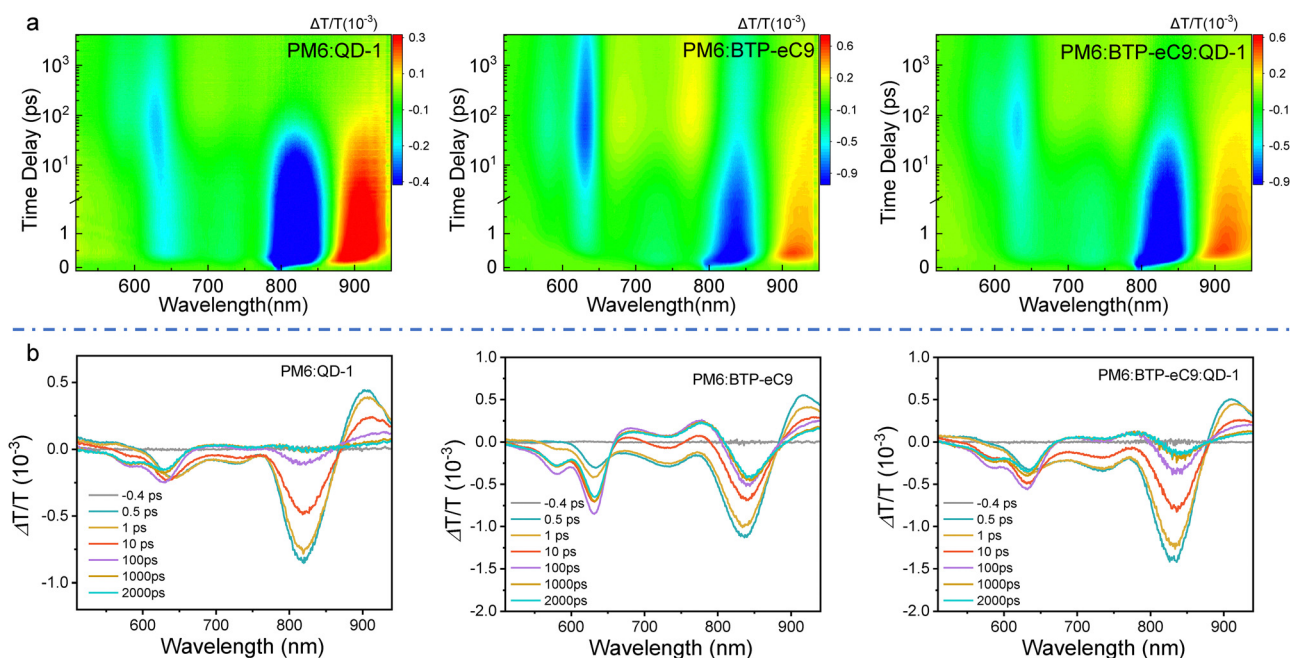


Fig. 5 (a) A color plot of the fs transient absorption spectra of PM6:QD-1, PM6:BTP-eC9, and PM6:BTP-eC9:QD-1 blended films under 800 nm excitation and (b) the representative fs transient absorption spectra of the PM6:QD-1, PM6:BTP-eC9, and PM6:BTP-eC9:QD-1 blended films at the indicated delay times under 800 nm excitation.

the blend films, we extracted the kinetic data at 630 nm (Fig. S26, ESI†) and applied biexponential fitting to obtain the characteristic time constants τ_1 and τ_2 . The fast τ_1 component is generally associated with hole transfer processes at the donor/acceptor interface, while the slower τ_2 component corresponds to excitons generated in the crystalline phase that need to migrate to the domain interface before dissociation.

As displayed in Table S7 (ESI†), the τ_1 and τ_2 for the PM6:QD-1, PM6:BTP-eC9, and PM6:BTP-eC9:QD-1 films are 0.28/11.53, 0.41/10.02, and 0.36/11.29 ps, respectively. The values of τ_1 and τ_2 in the ternary blend film fall within the range of those observed in the two binary blend films, suggesting that the morphology of the ternary blend is more suitable. These factors collectively contribute to the higher J_{sc} , FF, and PCE of the ternary device.

Conclusions

We designed a novel dimer acceptor, QD-1, featuring a large conjugated rigid skeleton. This dimer acceptor exhibited small reorganization energy, low energy disorder, and weak electron-photon coupling. With these advantages and the well-formed fibrillar morphology of the blend film, the PM6:QD-1-based binary OSC achieved a high PCE of 19.46%, the highest reported for binary devices using dimer acceptors. Notably, when QD-1 was incorporated into the PM6:BTP-eC9 blend, the ternary device achieved a PCE of 20.19% and demonstrated enhanced thermal stability. This improvement was attributed to enhanced exciton dissociation, reduced charge recombination and ΔE_{nr} , and improved carrier mobility compared to the binary device.

Furthermore, the ternary OSC exhibited a lower trap state density and a more optimized morphology than the binary devices, leading to enhanced PCE with simultaneously improved V_{oc} , J_{sc} , and FF. Finally, a large-area module with an active area of 13.5 cm² was fabricated and achieved an impressive PCE of 17.33%, which is at the leading level for large area modules. Our work demonstrates the significant potential of large conjugated rigid dimer acceptors for achieving high-efficiency and high-stability OSCs and will inspire further innovative exploration of such large conjugated rigid skeletons in OSCs.

Author contributions

W. S. wrote the original manuscript draft, performed the in-depth data analysis, tested the OSC devices, and obtained the EQE measurements. C. L. and Q. H. contributed to the material design and synthesis. W. Z. and G. L. carried out the theoretical computation. R. W., G. S., and X. C. provided experimental support for the femtosecond transient absorption, TPC, and TPV tests. L. L. prepared the large area module. Y. L. and Z. Y. assisted in the data analysis and manuscript revision. C. L., X. W., and Y. C. supervised and directed this project. All authors discussed the results and commented on the manuscript.

Data availability

The data that support the findings of this study are available from the corresponding author upon reasonable request.

Conflicts of interest

There are no conflicts to declare.

Acknowledgements

The authors gratefully acknowledge the financial support from the National Natural Science Foundation of China (52025033, 52373189, 52173010, 22361132530), and the Ministry of Science and Technology of China (2022YFB4200400).

References

- 1 J. Huang, Z. Lu, J. He, H. Hu, Q. Liang, K. Liu, Z. Ren, Y. Zhang, H. Yu, Z. Zheng and G. Li, *Energy Environ. Sci.*, 2023, **16**, 1251.
- 2 S. Li, Z. Li, X. Wan and Y. Chen, *eScience*, 2023, **3**, 100085.
- 3 R. Søndergaard, M. Hösel, D. Angmo, T. T. Larsen-Olsen and F. C. Krebs, *Mater. Today*, 2012, **15**, 36.
- 4 L. Meng, Y. Zhang, X. Wan, C. Li, X. Zhang, Y. Wang, X. Ke, Z. Xiao, L. Ding, R. Xia, H.-L. Yip, Y. Cao and Y. Chen, *Science*, 2018, **361**, 1094.
- 5 S. Guan, Y. Li, C. Xu, N. Yin, C. Xu, C. Wang, M. Wang, Y. Xu, Q. Chen, D. Wang, L. Zuo and H. Chen, *Adv. Mater.*, 2024, **36**, 2400342.
- 6 Y. Jiang, S. Sun, R. Xu, F. Liu, X. Miao, G. Ran, K. Liu, Y. Yi, W. Zhang and X. Zhu, *Nat. Energy*, 2024, **9**, 975.
- 7 L. Zhu, M. Zhang, G. Zhou, Z. Wang, W. Zhong, J. Zhuang, Z. Zhou, X. Gao, L. Kan, B. Hao, F. Han, R. Zeng, X. Xue, S. Xu, H. Jing, B. Xiao, H. Zhu, Y. Zhang and F. Liu, *Joule*, 2024, **8**, 3153.
- 8 Z. Chen, J. Ge, W. Song, X. Tong, H. Liu, X. Yu, J. Li, J. Shi, L. Xie, C. Han, Q. Liu and Z. Ge, *Adv. Mater.*, 2024, **36**, 2406690.
- 9 N. Wei, J. Chen, Y. Cheng, Z. Bian, W. Liu, H. Song, Y. Guo, W. Zhang, Y. Liu, H. Lu, J. Zhou and Z. Bo, *Adv. Mater.*, 2024, **36**, 2408934.
- 10 Z. Ge, J. Qiao, Y. Li, J. Song, X. Duan, Z. Fu, H. Hu, R. Yang, H. Yin, X. Hao and Y. Sun, *Angew. Chem., Int. Ed.*, 2025, **64**, e202413309.
- 11 H. Li, Y. Li, X. Dai, X. Xu and Q. Peng, *Angew. Chem., Int. Ed.*, 2024, **64**, e202416866.
- 12 Y. Sun, L. Wang, C. Guo, J. Xiao, C. Liu, C. Chen, W. Xia, Z. Gan, J. Cheng, J. Zhou, Z. Chen, J. Zhou, D. Liu, T. Wang and W. Li, *J. Am. Chem. Soc.*, 2024, **146**, 12011.
- 13 C. Li, G. Yao, X. Gu, J. Lv, Y. Hou, Q. Lin, N. Yu, M. S. Abbasi, X. Zhang, J. Zhang, Z. Tang, Q. Peng, C. Zhang, Y. Cai and H. Huang, *Nat. Commun.*, 2024, **15**, 8872.
- 14 Y. Yu, J. Wang, Z. Chen, Y. Xiao, Z. Fu, T. Zhang, H. Yuan, X.-T. Hao, L. Ye, Y. Cui and J. Hou, *Sci. China: Chem.*, 2024, **67**, 4194.

- 15 Y. Jiang, Y. Li, F. Liu, W. Wang, W. Su, W. Liu, S. Liu, W. Zhang, J. Hou, S. Xu, Y. Yi and X. Zhu, *Nat. Commun.*, 2023, **14**, 5079.
- 16 Z. Fu, J. W. Qiao, F. Z. Cui, R. H. Gui, P. Lu, H. Yin, X. Y. Du and X. T. Hao, *Adv. Mater.*, 2024, **36**, 2413317.
- 17 Y. Fu, L. Xu, Y. Li, E. J. Yang, Y. Guo, G. Cai, P. F. Chan, Y. Ke, C.-J. Su, U. S. Jeng, P. C. Y. Chow, J.-S. Kim, M.-C. Tang and X. Lu, *Energy Environ. Sci.*, 2024, **17**, 8893.
- 18 C. Zhang, S. Mahadevan, J. Yuan, J. K. W. Ho, Y. Gao, W. Liu, H. Zhong, H. Yan, Y. Zou, S.-W. Tsang and S. K. So, *ACS Energy Lett.*, 2022, **7**, 1971.
- 19 J. Zhou, D. He, Y. Li, F. Huang, J. Zhang, C. Zhang, Y. Yuan, Y. Lin, C. Wang and F. Zhao, *Adv. Mater.*, 2023, **35**, 2207336.
- 20 Z. Zhang, Y. Li, G. Cai, Y. Zhang, X. Lu and Y. Lin, *J. Am. Chem. Soc.*, 2020, **142**, 18741.
- 21 X. Meng, M. Li, K. Jin, L. Zhang, J. Sun, W. Zhang, C. Yi, J. Yang, F. Hao, G. W. Wang, Z. Xiao and L. Ding, *Angew. Chem., Int. Ed.*, 2022, **61**, e202207762.
- 22 J. Wang, X. Jiang, H. Wu, G. Feng, H. Wu, J. Li, Y. Yi, X. Feng, Z. Ma, W. Li, K. Vandewal and Z. Tang, *Nat. Commun.*, 2021, **12**, 6679.
- 23 H. Tian, Y. Luo, Z. Chen, T. Xu, R. Ma, J. Wu, G. Li, C. Yang and Z. Luo, *Adv. Energy Mater.*, 2024, 2404537.
- 24 C. Wang, Q. Chen, C. Zhang, B. Han, X. Liu, S. Liang, B. Wang, C. Xiao, B. Gao, Z. Tang, G. Lu, L. Ding and W. Li, *CCS Chem.*, 2025, **7**, 1177.
- 25 H. Chen, Y. Zou, H. Liang, T. He, X. Xu, Y. Zhang, Z. Ma, J. Wang, M. Zhang, Q. Li, C. Li, G. Long, X. Wan, Z. Yao and Y. Chen, *Sci. China: Chem.*, 2022, **65**, 1362.
- 26 Y. Lang, H. Lai, Y. Fu, R. Ma, P. W. K. Fong, H. Li, K. Liu, X. Yang, X. Lu, T. Yang, G. Li and F. He, *Adv. Mater.*, 2024, 2413270.
- 27 Z. Luo, W. Wei, R. Ma, G. Ran, M. H. Jee, Z. Chen, Y. Li, W. Zhang, H. Y. Woo and C. Yang, *Adv. Mater.*, 2024, **36**, 2407517.
- 28 Y. Shi, Y. Chang, K. Lu, Z. Chen, J. Zhang, Y. Yan, D. Qiu, Y. Liu, M. A. Adil, W. Ma, X. Hao, L. Zhu and Z. Wei, *Nat. Commun.*, 2022, **13**, 3256.
- 29 H. Wang, C. Cao, H. Chen, H. Lai, C. Ke, Y. Zhu, H. Li and F. He, *Angew. Chem., Int. Ed.*, 2022, **61**, e202201844.
- 30 F. Qi, Y. Li, R. Zhang, F. R. Lin, K. Liu, Q. Fan and A. K. Y. Jen, *Angew. Chem., Int. Ed.*, 2023, **62**, e202303066.
- 31 L. Zhang, Z. Zhang, D. Deng, H. Zhou, J. Zhang and Z. Wei, *Adv. Sci.*, 2022, **9**, 2202513.
- 32 J. Wan, T. Wang, R. Sun, X. Wu, S. Wang, M. Zhang and J. Min, *Adv. Mater.*, 2023, **35**, 2302592.
- 33 H. Chen, Z. Zhang, P. Wang, Y. Zhang, K. Ma, Y. Lin, T. Duan, T. He, Z. Ma, G. Long, C. Li, B. Kan, Z. Yao, X. Wan and Y. Chen, *Energy Environ. Sci.*, 2023, **16**, 1773.
- 34 K. Ma, H. Liang, Y. Wang, T. He, T. Duan, X. Si, W. Shi, G. Long, X. Cao, Z. Yao, X. Wan, C. Li, B. Kan and Y. Chen, *Sci. China: Chem.*, 2024, **67**, 1687.
- 35 S. Li, R. Zhang, M. Zhang, J. Yao, Z. Peng, Q. Chen, C. Zhang, B. Chang, Y. Bai, H. Fu, Y. Ouyang, C. Zhang, J. A. Steele, T. Alshahrani, M. B. J. Roeffaers, E. Solano, L. Meng, F. Gao, Y. Li and Z.-G. Zhang, *Adv. Mater.*, 2023, **35**, 2206563.
- 36 X. Liu, Z. Zhang, C. Wang, C. Zhang, S. Liang, H. Fang, B. Wang, Z. Tang, C. Xiao and W. Li, *Angew. Chem., Int. Ed.*, 2023, **63**, e202316039.
- 37 H. Chen, X. Cao, X. Xu, C. Li, X. Wan, Z. Yao and Y. Chen, *Chin. J. Polym. Sci.*, 2022, **40**, 921.
- 38 W. Shi, Q. Han, Y. Zhu, Y. Xia, T. He, S. Wang, L. Li, W. Ma, G. Long, G. Li, Z. Yao, C. Li, X. Wan and Y. Chen, *Natl. Sci. Rev.*, 2025, **12**, nwae409.
- 39 Z. Yao, X. Wan, C. Li and Y. Chen, *Acc. Mater. Res.*, 2023, **4**, 772.
- 40 X. Ji, T. Wang, Q. Fu, D. Liu, Z. Wu, M. Zhang, H. Y. Woo and Y. Liu, *Macromol. Rapid Commun.*, 2023, **44**, 2300213.
- 41 R. A. Marcus, *Angew. Chem., Int. Ed. Engl.*, 1993, **32**, 1111.
- 42 L. Zhan, S. Li, Y. Li, R. Sun, J. Min, Z. Bi, W. Ma, Z. Chen, G. Zhou, H. Zhu, M. Shi, L. Zuo and H. Chen, *Joule*, 2022, **6**, 662.
- 43 X. Gu, Y. Wei, N. Yu, J. Qiao, Z. Han, Q. Lin, X. Han, J. Gao, C. Li, J. Zhang, X. Hao, Z. Wei, Z. Tang, Y. Cai, X. Zhang and H. Huang, *CCS Chem.*, 2023, **5**, 2576.
- 44 M. de Jong, L. Seijo, A. Meijerink and F. T. Rabouw, *Phys. Chem. Chem. Phys.*, 2015, **17**, 16959.
- 45 S. R. Forrest, *Organic Electronics: Foundations to Applications*, Oxford University Press, 2020.
- 46 M. Zhang, Z. Wang, L. Zhu, R. Zeng, X. Xue, S. Liu, J. Yan, Z. Yang, W. Zhong, G. Zhou, L. Kan, J. Xu, A. Zhang, J. Deng, Z. Zhou, J. Song, H. Jing, S. Xu, Y. Zhang and F. Liu, *Adv. Mater.*, 2024, **36**, 2407297.
- 47 T. D. Krauss and F. W. Wise, *Phys. Rev. B: Condens. Matter Mater. Phys.*, 1997, **55**, 9860.
- 48 V. Coropceanu, M. Malagoli, D. A. da Silva Filho, N. E. Gruhn, T. G. Bill and J. L. Brédas, *Phys. Rev. Lett.*, 2002, **89**, 275503.
- 49 S. Liu, J. Yuan, W. Deng, M. Luo, Y. Xie, Q. Liang, Y. Zou, Z. He, H. Wu and Y. Cao, *Nat. Photonics*, 2020, **14**, 300.
- 50 Y. Cui, H. Yao, J. Zhang, K. Xian, T. Zhang, L. Hong, Y. Wang, Y. Xu, K. Ma, C. An, C. He, Z. Wei, F. Gao and J. Hou, *Adv. Mater.*, 2020, **32**, 1908205.
- 51 A. K. K. Kyaw, D. H. Wang, C. Luo, Y. Cao, T.-Q. Nguyen, G. C. Bazan and A. J. Heeger, *Adv. Energy Mater.*, 2014, **4**, 1301469.
- 52 P. Schilinsky, C. Waldauf and C. J. Brabec, *Appl. Phys. Lett.*, 2002, **81**, 3885.
- 53 R. Wang, C. Zhang, Q. Li, Z. Zhang, X. Wang and M. Xiao, *J. Am. Chem. Soc.*, 2020, **142**, 12751.